3D restoration microscopy improves quantification of enzyme-labeled fluorescence-based single-cell phosphatase activity in plankton

Diaz-de-Quijano, Daniel ; Palacios, Pilar ; Horňák, Karel ; Felip, Marisol

Abstract: The ELF or fluorescence-labeled enzyme activity (FLEA) technique is a culture-independent single-cell tool for assessing plankton enzyme activity in close-to-in situ conditions. We demonstrate that single-cell FLEA quantifications based on two-dimensional (2D) image analysis were biased by up to one order of magnitude relative to deconvolved 3D. This was basically attributed to out-of-focus light, and partially to object size. Nevertheless, if sufficient cells were measured (25-40 cells), biases in individual 2D cell measurements were partially compensated, providing useful and comparable results to deconvolved 3D. We also discuss how much caution should be used when comparing the single-cell enzyme activities of different sized bacterio- and/or phytoplankton populations measured on 2D images. Finally, a novel method based on deconvolved 3D images (wide field restoration microscopy; WFR) was devised to improve the discrimination of similar single-cell enzyme activities, the comparison of enzyme activities between different size cells, the measurement of low fluorescence intensities, the quantification of less numerous species, and the combination of the FLEA technique with other single-cell methods. These improvements in cell enzyme activity measurements will provide a more precise picture of individual species' behavior in nature, which is essential to understand their functional role and evolutionary history.

DOI: https://doi.org/10.1002/cyto.a.22486

Cytometry, Part A

3D restoration microscopy improves quantification of enzyme-labelled fluorescence (ELF)-based single-cell phosphatase activity in plankton

Journal:	*Cytometry: Part A*
Manuscript ID:	13-088.R2
Wiley - Manuscript type:	Original Article
Date Submitted by the Author:	n/a
Complete List of Authors:	Diaz-de-Quijano, Daniel; University of Barcelona-CEAB-CSIC, Department of Ecology Palacios, Pilar; CSIC, Centro Nacional de Biotecnología Horňák, Karel; University of Zurich, Limnological Station of the Institute of Plant Biology; Biology Centre of the Academy of Sciences of the Czech Republic, Institute of Hydrobiology Felip, Marisol; University of Barcelona-CEAB-CSIC, Department of Ecology
Key Words:	3D fluorescence microscopy, deconvolution, ELF phosphate, phosphatase activity, phytoplankton

TITLE

3D restoration microscopy improves quantification of enzyme-labelled fluorescence (ELF)-based single-cell phosphatase activity in plankton

AUTHORS

Daniel Diaz-de-Quijano[a*], Pilar Palacios[b], Karel Horňák[c], Marisol Felip[a]

[a]Unitat de Limnologia, Departament d'Ecologia i Centre de Recerca d'Alta Muntanya, CEAB-CSIC-Universitat de Barcelona, Av. Diagonal 643, 08028 Barcelona, Catalonia, Spain.

[b]Centro Nacional de Biotecnología-CSIC, Darwin 3, Campus de Cantoblanco, 28049 Madrid, Spain.

[c]Biology Centre of the Academy of Sciences of the Czech Republic, Institute of Hydrobiology, Na Sádkách 7, CZ-370 05 České Budějovice, Czech Republic.

RUNNING HEADLINE

3D ELF single-cell phosphatase quantification

CONTACT INFORMATION

*Corresponding author. Present address: Departament d'Ecologia Universitat de Barcelona, Av. Diagonal 643, 08028 Barcelona, Catalonia, Spain. Tel.: +34 93 403 11 90. Fax: +34 93 411 14 38. E-mail address: diazdequijano@ub.edu (D. Diaz de Quijano)

CREDITS FOR RESEARCH SUPPORT

The study was supported by the Spanish Ministry of Science and Technology, projects TRAZAS (CGL2004-02989), ECOFOS (CGL2007-64177/BOS) and GRACCIE (CDS2007-00067).

ABSTRACT

The ELF or fluorescence-labelled enzyme activity (FLEA) technique is a culture-independent single-cell tool for assessing plankton enzyme activity in close-to-*in situ* conditions. We demonstrate that single-cell FLEA quantifications based on two-dimensional (2D) image analysis were biased by up to one order of magnitude relative to deconvolved 3D. This was basically attributed to out-of-focus light, and partially to object size. Nevertheless, if sufficient cells were measured (25 to 40 cells), biases in individual 2D cell measurements were partially compensated, providing useful and comparable results to deconvolved 3D. We also discuss how much caution should be used when comparing the single-cell enzyme activities of different sized bacterio- and/or phytoplankton populations measured on 2D images. Finally, a novel method based on deconvolved 3D images (wide field restoration microscopy; WFR) was devised to improve the discrimination of similar single-cell enzyme activities, the comparison of enzyme activities between different size cells, the measurement of low fluorescence intensities, the quantification of less numerous species, and the combination of the FLEA technique with other single-cell methods. These improvements in cell enzyme activity measurements will provide a more precise picture of individual species' behaviour in nature, which is essential to understand their functional role and evolutionary history.

KEY WORDS

3D fluorescence microscopy, deconvolution, ELF phosphate, phosphatase activity, phytoplankton

INTRODUCTION

Phosphorus recycling in ecosystems is driven by different processes involving various enzyme activities. Phosphatases (including phosphoesterases, nucleases and nucleotidases) hydrolyse oxygen–phosphorus bonds in phosphoesters, the dominant form of dissolved organic phosphorus (1–4), whereas C-P lyases and hydrolases hydrolyse carbon–phosphorus bonds in phosphonates (5). These enzymes may play a key role in those ecosystems in which P is temporarily or permanently a limiting factor, as is the case of some freshwater, marine and terrestrial ecosystems (6–10). Notably, P limitation is expected to increase as the deposition of atmospherically transported anthropogenic N modifies the N:P stoichiometry of ecosystems all over the world (11). A number of studies have already assessed the shifts in environmental enzyme activity driven by anthropogenic atmospheric N deposition (12,13) and by other parameters related to climate change that can modulate enzymatic activity, such as pH (14,15), temperature (16,17), and UV radiation (18–21). These studies have demonstrated the importance of enzyme activity in the response of ecosystems to global climate change. However, a more accurate characterization of the link between taxonomic identity and *in situ* enzymatic activity is essential to understand and to predict enzyme dynamics in nature.

Phosphomonoesterases are one of the most widely studied enzymes in aquatic ecosystems, and to date the only ones that can be assessed using the enzyme-labelled fluorescence-phosphate (ELFP) substrate, via the so-called FLEA technique. Upon enzymatic hydrolysis, the ELFP substrate is converted to a fluorescent ELF alcohol (ELFA) that precipitates at the site of enzyme activity (22). Therefore, the FLEA technique constitutes a powerful and culture-independent tool with which to study the

contribution of this functional trait to the species trophic strategy (23,24) at the single-cell level, and in close-to-*in situ* conditions. Simultaneously, this technique also enables the preservation of useful cell structures required for adequate taxonomic identification (autofluorescent chloroplasts and stained DNA), mainly in phyto- and bacterioplankton communities (25–28). Moreover, Nedoma and colleagues (29) developed a method to quantify the ELFA precipitate based on epifluorescence microscopy and 2D image analysis. Thus, the FLEA technique has provided the opportunity to open the "black box" of environmental enzyme activity in phyto- and bacterioplankton. Knowledge of single-cell enzymatic activity, if accurate enough, is essential for the proper definition of functional niches, the reconstruction of the evolution of functional traits associated with certain trophic strategies (30,31), and better modelling and understanding of the dynamics of enzyme activity in nature (32). Nonetheless, the 2D images on which most quantifications have been based to date are distorted representations of real 3D cells. Therefore, we hypothesized that (i) 2D image-based measurements might be significantly biased, and (ii) cell size might modulate this bias, which could invalidate comparisons between different size cells, such as phytoplankton and bacterial cells.

To test these hypotheses, a 3D imaging system was required. Amongst the different modalities of fluorescence microscopy (wide-field, structured light illumination, confocal, and confocal-derived techniques), 3D wide-field restoration microscopy (WFR) was chosen for several reasons. Blurring of light is a common phenomenon in all the abovementioned 3D microscopy techniques but it is especially important in 3D wide-field microscopy, where light blurs mainly along the Z axis and more moderately in the XY plane (33). This problem may be solved in one of two ways or via combination of approaches. On the one hand, mechanical devices may be used to reduce

the amount of out-of-focus light (confocal and structured light illumination microscopy). On the other hand, out-of-focus light may be considered informative light and any of the mentioned techniques, including wide-field, may be combined with image restoration by deconvolution to relocate out-of-focus light to its source (34). Secondly, the WFR imaging system requires a wide-field microscope with a motorized Z axis, a cooled digital CCD camera and deconvolution software for image restoration. This WFR set up is cheaper than that required for the other techniques and makes it affordable for a larger number of laboratories. Moreover, WFR microscopy is the most suitable technique for our fluorescence intensity quantification purposes and for microplankton samples (thin and with no or small amounts of fluorescent material out of focus). This technique has a higher signal-to-noise ratio (SNR) than laser scanning confocal microscopy (LSCM) for samples <30 µm thick (33,35), and uses CCD detectors with a quantum efficiency of ~60%, contrasting with that of photomultiplier (PMT) detectors normally used in confocal microscopy which used to have a quantum efficiency of ~10% (36). WFR microscopy also has the shortest acquisition time, which makes this technique a better option for fluorescence quantification and the imaging of living cells, as photobleaching of fluorophores and cell damage are minimized. Finally, WFR microscopy has also been found to be more sensitive and accurate than LSCM when measuring low fluorescence intensity objects (35,36), although ELFA labellings are usually intense enough for both techniques. So, although structured light illumination could be an alternative option (it meets most of the requirements mentioned above and has been reported to be reliable (37)), WFR is an appropriate choice for fluorescence quantification in phyto- and bacterioplankton samples.

In WFR, image formation can be described by the 3D mathematical model:

$$\text{image} = \text{object} \otimes \text{psf} \quad (1)$$

where *image* is the acquired image, *object* is the real specimen and *psf* is the point spread function of the microscope (all the elements in the equation are 3D arrays). The *psf* describes the way an infinitely small point would be imaged, and distorted, by the microscope (in fact, it is a 3D photograph of a subresolution fluorescent bead) (38). By the mathematical operation of convolution ($\otimes$), i.e. by applying the psf to every single point in the real 3D object, we would get the blurred image. Inversely, an estimate of the object can be calculated by deconvolution of the distorted image. Two kinds of deconvolution algorithms have been implemented: deblurring and restoration algorithms (38–40). The first operate separately on each focal plane of the 3D image to estimate and eliminate its blur. In contrast, restoration algorithms consider all the 3D data simultaneously to reassign light to its source in its original in-focus plane. The result in both cases is a contrast improvement but only the latter algorithms respect all the acquired information and are, therefore, suitable for improving fluorescence intensity measurements (33,35,41).

In this study, we describe and propose a novel method for accurate FLEA quantification in phytoplankton cells based on WFR. We characterize the improvement in performance and accuracy of the proposed imaging system, and we compare, for the first time in the literature, 2D and 3D WFR fluorescence intensity quantifications. This is an important contribution because on the one hand 3D fluorescence microscopy is considered superior to 2D and is thus widely used for many different purposes (41–43), but on the other hand, 2D imaging may still be used given its various advantages: simplicity, faster acquisition and analysis times, cheaper equipment and lower storage memory requirements. With this in mind, we describe the errors associated with the current 2D

wide-field method and the relative distorting effect of cell size on these measurements, and discuss how to correctly interpret 2D-based data.

MATERIALS AND METHODS

Study sites and sampling

Data were collected from phytoplankton cells from eight high mountain lakes of the Central Pyrenees in order to have a wide range of phosphatase activity and cell sizes.

FLEA phosphatase protocol

Samples were sieved in the field to remove zooplankton and processed upon arrival at the laboratory (always within 6 hours after sampling in summer and within 18 hours in winter and spring). An aliquot per sample was fixed with alkaline Lugol for phytoplankton determination. The FLEA technique was performed as previously described by Diaz-de-Quijano & Felip (44). Liquid samples were incubated in the dark, at *in situ* temperature, buffered at *in situ* pH with 0.1M HCl/Tris, citric or acetic acid buffers depending on sample pH, and using 10 µM of ELFP (Molecular Probes, E6589) substrate to achieve a compromise concentration above K_M for almost all samples. The time courses of the incubations were always monitored by fluorimeter to ensure that we sampled the incubation during its linear phase, as previously recommended (29). Incubation of the samples was stopped by gentle filtration (<20 KPa) through 2 µm pore polycarbonate filters, following which the samples were stored at -20ºC until they were mounted with CitiFluor AF1, and covered with 0.17 µm thick cover slides for microscope analysis.

Beads

Different sets of fluorescent beads were quantified: 2.5 µm diameter fluorescence intensity calibrated beads (In Speck™ Green (505/515) Microscope Image Intensity Calibration Kit, 2.5 µm, Invitrogen, Molecular Probes, I7219), 6 µm beads (FocalCheck

Fluorescent Microspheres Kit, 6 µm, Slide C, Invitrogen, Molecular Probes, F24633), and 15 µm beads (FluoSpheres polystyrene microspheres, 15 µm, yellow-green fluorescent (505/515), Invitrogen, Molecular Probes, F8844). A drop of each intensity and size set of beads was spread separately on a slide, air-dried, and mounted with CitiFluor AF1 as in the case of phytoplankton cells except for the 6 µm beads, which were commercially mounted in optical cement.

Beads were used to check for size and intensity effect. First, we measured 193 fluorescent 2.5 µm diameter latex beads stained with six different calibrated intensities ranging between three orders of magnitude by flow cytometry (as a reference) and by quantitative microscopy (2D raw, and 3D raw or deconvolved). We compared differences in relative fluorescence measurements between the different methods and checked for linearity of the fluorescence intensity measurements using simple linear regression, within the R environment. The percentages of FU were log transformed to meet the assumptions of normality and homoscedasticity. Secondly, we used linear regression to relate 2D and 3D measurements of different size beads. Sample sizes were n=30 for 15 µm beads, n=52 for 6 µm beads and n=140 for 2.5 µm beads. We estimated the regression slopes and calculated their two-sided and nonparametric bootstrapped 95% confidence intervals with the boot.ci function in R, based on 10000 replicates (samplings of data) each. The bias-corrected accelerated percentile (BCa) interval type was chosen (45,46).

Flow cytometry

Intensity calibrated fluorescent beads (as detailed above) diluted in 1 ml of fresh 0.2 µm-filtered Milli-Q water were measured using the FACSCalibur flow cytometer

(Becton Dickinson, USA) equipped with an air-cooled argon ion laser (15 mW, 488 nm). Beads were identified based on their fluorescent intensity signatures in a plot of 90° angle light scatter versus green fluorescence (515 nm) using the flow cytometry analysis software CELLQuest Pro (Becton Dickinson). To avoid particle coincidence, the rate of particle passage was kept at <1000 events s^{-1} during analyses.

Image acquisition

Samples were imaged with a Huygens restoration microscope (Scientific Volume Imaging b. v., Hilversum, The Netherlands) built around a Nikon Eclipse 90i epifluorescence microscope (Nikon, Tokyo, Japan). The microscope was equipped with a monochromatic Vosskühler COOL-1300Q CCD camera with a pixel size of 6.45 μm^2 (Vosskühler GmbH, Osnabrück, Germany) and a Xenon-arc illumination. Bead images were acquired with a Plan Apo 40X/1.0 NA oil immersion objective lens and a fluorescein filter block (ex. 450–490 nm, em. >515 nm). Cell images were acquired using a Plan Fluor 20X/0.75 NA MI objective lens with the collar adjusted to immersion with oil, and two different filter blocks: an ELFA-specific filter block (ex. 360–370 nm, em. 520–540 nm) and a chlorophyll-specific filter block (ex. 510–550 nm, em. >590 nm) for species determination. A 9.4% w/v fluorescein standard solution was used for shading correction, and to determine an inter-session correction factor (*Icf*) (47). Gain was fixed to 1 but exposure time was modified for each image acquisition to avoid image clipping (no voxel saturation was allowed) and also to collect as much information as possible from weakly bright voxels. Modulation of exposure time between images did not hinder comparability because CCDs generate a linear response over time (48). The three parameters were recorded in metadata for further calculations. Collected 3D images were a stack composed of 35 2D slides spaced at a distance similar

to the depth of field (DOF) (1.4 µm at the 20X objective and 0.7 µm at the 40X objective), and had the object of interest centred on the Z axis.

Deconvolution

Image restoration (deconvolution) was performed using the Classic Maximum Likelihood Estimation algorithm implemented in Huygens Professional 3.3.2p1, which includes a batch processor. Images were translated from nd2 to ICS file format to import them into the deconvolution software. They were cropped, respecting the volume dimensions of out-of-focus light, to speed up deconvolution. A set of images with known SNR of 40, 30, 20 and 10 was visually compared with our raw images to determine their SNR index. A SNR index of 35 was used according to our data, the maximum number of iterations was set to 40, and bleaching correction was activated. In order to select a point spread function (PSF) we deconvolved an image of a 2.5 µm fluorescent bead using both, experimental and theoretical PSF. The latter was able to reconstruct the known spherical shape of the fluorescent bead whereas the former produced a distorted shape (double banana-shaped artefact at the top and bottom edges). Moreover, the grey values of the deconvolved images showed a quantitatively more efficient deconvolution when using theoretical PSF (minimum, mean and maximum) (0, 38.03, 40807) than experimental PSF (0.002, 16.55, 13481). Therefore, we decided to use the theoretical PSF for both reasons: it triggered a better shape and fluorescence intensity restoration. The output format file had to be scaled 16 bit TIFF because the NIS-Elements software used to quantify the images only supports up to 16 bit images, whereas voxel intensities reached values above 16 bits after deconvolution.

Image analysis and calculations

Fluorescence intensity was measured using NIS-Elements AR 2.34 software (Laboratory Imaging, Praha, Czech Republic). We used two macros to semi-automate the quantification routine: the macro described by Nedoma *et al*. (29) for 2D images, and an adapted version for 3D images. In the latter macro, the user is able to set an optimum contrast enhancement and move across the different slides of the stack to properly select the area of the object and the area of the background to be measured. These areas are projected across the whole stack defining two irregular prisms (the Volumes of Interest, VOIs). Finally, the macro measured the following variables per slide in the stack: area of the object (*Area*; μm^2), mean grey value of the object (*Mgv*; dimensionless), and mean grey value of the background (*BgMgv*; dimensionless). These measurements were automatically exported to an Excel file for semi-automated calculation together with the following metadata: distance between slides in a stack (*Zstep*; µm), number of slides (*ns*; dimensionless), camera exposure time (*expT*; ms), camera gain (*Gain*; dimensionless), intersession correction factor (*Icf*; dimensionless), and image file identity. The relative fluorescence of the object (*RFobject*; fluorescence units –FU) was calculated as follows:

$$RFobject = \frac{Icf}{\exp T \cdot Gain} \cdot \sum_{i=1}^{ns} Area \cdot Zstep \cdot (Mgv_i - BgMgv_i) \quad (2)$$

A conversion factor to relate the amount of ELFA to FU (*ConvF*; fmol ELFA·FU^{-1}) was obtained from the comparison of fluorimeter and microscope raw 2D measurements. The increase in ELFA fluorescence of several phosphatase incubations from an independent set of samples was measured by both methods in parallel. Microscope measurements were expressed in FU whereas fluorimeter measurements were translated to fmol ELFA using a calibration line based on a dilution of commercially available

ELFA standard. See Nedoma *et al*. (29) for more details. In order to obtain the *ConvF* for the raw 3D and deconvolved 3D modes, we compared the fluorimeter measurements (fmol ELFA) and predicted raw and deconvolved 3D fluorescence intensity values corresponding to the raw 2D measurements of the independent set of samples. This prediction was based in two partial regressions (built on the 212 raw, or 175 deconvolved, cells measured in this study) that related raw 2D fluorescence intensity and object area to the raw (or deconvolved) 3D fluorescence intensity. *ConvF* values were 0.013553 fmol ELFA·FU^{-1} (raw 2D), 0.000124 fmol ELFA·FU^{-1} (raw 3D), and 0.000014 fmol ELFA·FU^{-1} (deconvolved 3D). In the case of phytoplankton cells, the single cell hydrolysed phosphate (*SCHP*; fmol ELFA·$cell^{-1}$) was calculated as:

$$SCHP = RFobject \cdot ConvF \quad (3)$$

Finally, the single cell phosphatase activity (SCPA; fmol ELFA·$cell^{-1}$·h^{-1}) was calculated by dividing SCHP by the number of hours in the linear phase before incubation was stopped.

Statistics

Linear least-squares regression, partial correlation, partial regression, graphics and variation partitioning were carried out in the R environment (49). Comparison of least-squares regression slopes and comparison of slopes to a theoretical value for the different intensity beads were performed using GraphPad Prism 5.01 for Windows (GraphPad Software, Inc., San Diego, CA, USA). K-means analysis was performed within the Ginkgo multivariate analysis system (http://biodiver.bio.ub.es/ginkgo/index.html, Barcelona, Catalonia).

We used an iterative approach in the R environment to find the minimum number of cells that must be counted in raw 2D to obtain the most similar results to deconvolved 3D. For each group (a species or a set of several species), the first loop involved removing one cell per iteration, sampled stochastically without replacement, and testing if the new set of sampled data: (i) maintained the homogeneity of variances between raw 2D and deconvolved 3D, and (ii) had the same difference in raw 2D and deconvolved 3D means as calculated using all observations. The macro recorded the number of remaining cells (sample size) when conditions (i) or (ii) were not met. The second loop restarted the first one 10000 times and recorded the results. For each species (or set of several species), we considered the minimum sampling size to be the number of cells that did not significantly alter the original mean and SD results in 99.99% of iterations.

RESULTS

Measurement of beads of different fluorescence intensity

We measured 193 fluorescence intensity calibrated latex beads of 2.5 μm diameter using three image analysis methods: raw 2D, raw 3D and deconvolved 3D (Table 1). These measurements were compared with flow cytometry measurements with adjusted R-squared values between 0.994 and 0.9969 and slopes between 0.9830 and 1.0199. These slopes were significantly different from 1 (p-value<0.05), but approached 1 in 3D imaging (raw or deconvolved). Therefore, the tested quantitative microscopy methods provided comparable but slightly different relative fluorescence intensity measurements to those obtained by flow cytometry (Fig. 1 a).

We also compared the previously used raw 2D IA method to the two 3D methods. Raw 3D provided the same relative fluorescence measurements as raw 2D (slope=1, $\alpha=0.05$) (Fig. 1 b). Deconvolved 3D did not fit a linear regression (runs test p-value<0.0001) but did fit a quadratic one when low intensity beads were included (Fig. 1 c). This was due to a difference between the two methods when measuring low intensity objects. If the latter objects were excluded, the relationship became linear (Fig. 1 d). Deconvolved 3D measurements provided the most similar percentage fluorescence to that obtained by flow cytometry in these dimmest fluorescent beads (although not in the intermediate intensity beads) (Table 1).

Measurement of different size fluorescent beads

Fluorescence intensities of 2.5, 6 and 15.4 μm diameter beads were quantified by the raw 2D, raw 3D and deconvolved 3D methods. The slopes of simple regression lines that related 2D and 3D methods increased along with the diameter of the bead, which

suggests that object size might determine the relationship between the raw 2D and the 3D measurements. This tendency was clearer when comparing raw 2D vs. raw 3D than raw 2D vs. deconvolved 3D, because the 95% confidence intervals of the regression's slopes overlapped in the latter case (Table 2).

Measurement of phytoplankton cells

We quantified SCHP (fmol·cell^{-1}) in lake phytoplankton cells using the previously outlined quantitative microscopy methods. Cells were divided into three size groups by a K-means analysis. The plots relating the current method (raw 2D) to the 3D methods (Fig. 2 a,b) confirmed the results obtained by measuring different size beads. The relationship between raw 2D and 3D gave regression lines for the different cell size groups with clearly different intercepts (Fig. 2 a), whereas that of raw 2D against deconvolved 3D was not as clearly affected by cell size. In this case, the increase in dispersion may mask any eventual cell size effect.

To understand the dispersion difference between Fig. 2 a and b we may consider an ideal cell (Fig. 2 right). Three-dimensional measurements are based on the sum of voxel intensities within a volume of interest (VOI). This volume is a prism whose irregular base is user-defined following the silhouette of the cell projected on the XY plane. Besides, the restoration algorithm that we used respects the total amount of energy that belonged to a cell in the raw image and simply relocates it to its source, in such a way that the sum of energy inside ($_i$) and outside ($_o$) the VOI before ($_r$) and after deconvolution ($_d$) is identical, i.e.:

$$E_{ir}+E_{or}=E_{id}+E_{od} \quad (4)$$

which can be expressed as:

$$E_{or}-E_{od}=E_{id}-E_{ir} \quad (5)$$

The dispersion difference between Fig. 2 a and b indicates that for two cells with a very similar raw 2D measurement, the difference for each cell between deconvolved 3D (E_{id}) and raw 3D (E_{ir}) values may be quite substantial. Taking into account equation 5, this dispersion difference also means that the difference of energy outside the VOI in the raw image (E_{or}) minus energy outside the VOI in the deconvolved image (E_{od}) differs between cells. Because the first element of the difference (E_{or}) is proportional to the degree of out-of-focus light and the second (E_{od}) is inversely proportional to the efficiency of deconvolution, we argue that the increase in dispersion observed when deconvolving could be due to either the original amount of acquired out-of-focus light, the efficiency of deconvolution or a combination of both. To further deepen our knowledge on this subject, we conducted a cell-by-cell inspection of the intensity profile of their VOI along the Z axis (Fig. 2). Only cells with sharp profiles, indicative of efficient deconvolution, were considered while those with inefficient deconvolution were excluded from the analysis (Fig. 2 c). (A total of 175 cells out of 212 were analysed). Thus, the increase in dispersion can be caused by actual differences in the amount of out-of-focus light between individual cells and not by any artefact introduced by deconvolution. As the magnitude of dispersion was virtually identical (Fig. 2 b and c), we were able to confirm that for a given value in raw 2D (or 3D), a range of values spanning one order of magnitude was recorded by deconvolved 3D. Therefore, raw SCHP measurements (used to calculate the population averages reported in recent studies) may be biased by up to one order of magnitude since out-of-focus light was not taken into account.

Since we used mismatching immersion oil (n=1.516 at 23ºC) and embedding Citifluor AF1 (n=1.4628 at 22ºC), it could be hypothesized that the increase in dispersion observed between raw and deconvolved results (Fig. 2 a and b) was also explained by the fact of having imaged under SA conditions. SA implies both, a strong decay in signal intensity as the focal plane is moved into the sample (depth aberration) and a challenge to efficient deconvolution. Nevertheless, only the former effect was to be taken into account because efficient deconvolutions triggering sharp and symmetric fluorescence intensity profiles where achieved thanks to a series of pre-deconvolution treatments (accurate image cropping to accommodate all the out-of-focus light, instable illumination correction, and correction of bleaching- and SA-induced fluorescence intensity decline in depth) together with a SA correction mechanism in Huygens Professional software (where the PSF was resized, and the whole image stack was splitted into a series of bricks along the Z axis to be able to apply different PSF to them). In the case that such dispersion was induced by SA the cells with high residuals in the 2D vs deconvolved 3D regression should be those closer to the coverslide because the loss of fluorescence intensity with depth is steeper there, and hence the pre-deconvolution bleaching (and SA) correction may increase more the whole 3D image intensity. Sample depth was recorded just for big and small beads, and we found that fifteen µm fluorescent beads also showed this increase in dispersion when deconvolved but there wasn't any significant correlation between sample depth and the residuals (Fig. 3). Therefore, difference in the dispersion between raw and deconvolved data does not seem to be caused by SA, either.

Additionally, we compared beads and cells to check whether morphology could be responsible for some of the unexplained variation. The adjusted R-squared of linear

regressions relating 2D and 3D measurements decreased when 3D was deconvolved, i.e. the unexplained variation increased . Concretely, the unexplained variation increase was high for 15µm beads, intermediate in the three populations of cells (large, medium and small) with diverse morphology (including diatoms, dinoflagellates, chrysophytes and chlorophytes), and small in the case of 2.5µm beads. Hence, morphology might not be an important driver of unexplained variation.

To assess the impact of the cell area on the relationship between 2D and 3D fluorescence intensity measurements, we developed a specific model. Since 2D and 3D measurements are different ways of measuring fluorescence intensity, these variables were highly correlated. Log of area vs. log of raw 3D fluorescence intensity and log of area vs. log of deconvolved 3D fluorescence intensity had partial correlation coefficients of 0.997 and 0.93, respectively. Due to this high degree of collinearity, partial regression was selected as the best approach to forecast raw ($Raw3D_0$) or deconvolved ($Dec3D_0$) 3D measurements from new area ($Area_0$) and 2D measurements ($Raw2D_0$). The e subindices ($_e$) correspond to estimated intermediate variables necessary to resolve the equation system. The functions we obtained, as the log of area (μm^2) and log of fluorescence intensity expressed as SCHP (fmol ELFA·$cell^{-1}$), were:

$$Raw2D_e = Raw2D_0 - (-1.482449 + (1.329476 \cdot Area_0))$$

$$Raw3D_e = 1.255279 \cdot 10^{-17} + (1.026991 \cdot Raw2D_e)$$

$$Raw3D_0 = Raw3D_e + (-2.406128 + (1.514223 \cdot Area_0))$$

(6)

And in the case of deconvolved 3D:

$$Raw2D_e = Raw2D_0 - (-2.259155 + (1.725148 \cdot Area_0))$$

$$Dec3D_e = 2.037851 \cdot 10^{-17} + (8.952034e\text{-}01 \cdot Raw2D_e)$$

$$Dec3D_0 = Dec3D_e + (-2.145553 + (1.600514 \cdot Area_0))$$

(7)

Then, we calculated adjusted R-squared to clarify whether the addition of object size (*Area*) provided any improvement in the explanation of variation relative to a simple linear regression that excluded object size. The results showed that for the forecast of raw 3D, we explained 99.5% of the variation when using a linear regression without the *Area* variable, whereas the explained variation increased to 99.7% when the *Area* variable was included in the partial regression. In contrast, for the forecast of deconvolved 3D, the inclusion of the *Area* variable slightly decreased the explained variation (from 95.4% to 95.3%). The partitioning of variation is summarized in Table 3, and confirms the results based on different size beads: object size slightly biases raw 2D measurements when compared to raw 3D, but this size effect is masked when compared to deconvolved 3D because the increase in unexplained variation (4.5–0.2), which is attributable to deconvolution, is almost 150 times greater than the variation explained by object size alone (0.03).

Here again, we could hypothesize that the slight impact of the cell area on the relationship between 2D and 3D fluorescence intensity measurements (Fig. 2 a) was influenced by the fact of having imaged under SA conditions. To test this hypothesis, we used *in silico* modelling. The behaviour of the ratio between raw 2D and raw 3D fluorescence intensity values (2D/3D) was observed for typical intensity profiles of

small and big objects at different distances to the coverslide. As we mentioned above, the decline of fluorescence intensity in depth caused by SA is steeper in the first micrometers and more moderate at deeper positions in the sample. This triggered two observable phenomena: (i) the 2D/3D was slightly smaller than in the cases where the decline was lineal or where there wasn't any decline, and (ii) the 2D/3D relationship diminished more intensely when the non-aberrated intensity profile of the object was flatter (not sharply unimodal), but mainly diminished when the imaged object was closer to the coverslide (steeper loss of intensity). Because big cells usually have flatter intensity profiles than small cells, it was expectable that big cells had smaller 2D/3D than small cells (as it was observed in Fig. 2 a), and especially when the cells were close to the coverslide. Therefore, it is possible that SA contributed to some extent to the apparent size effect, although it would be quantitatively modest according to the model (to a maximum of about 5% in an extreme case).

In order to assess the bias induced by cell size in raw 2D single-cell enzyme activity measurements, raw 2D SCHP were determined for five ideal spherical cells ranging from 2 to 32 µm diameter and having the same deconvolved 3D SCHP value by using equation 7. The different raw 2D values of these cells were compared in pairs and the comparison was expressed as a percentage (Table 4). If cells with 2 and 32 µm in diameter were compared in raw 2D (the most extreme case), it could seem that the larger cell had 71% of the SCHP of the small cell (i.e. the small cell had 142% of the SCHP of the large cell), while they would have the same value in deconvolved 3D according to our model.

Species level analysis

In the analysis of natural populations or species, it is interesting to assess the population- or species-specific functional variability as well as the average SCPA. Three selected species of lake phytoplankton were analysed for SCHP to estimate enzymatic functional variability by the three techniques (raw 2D and raw or deconvolved 3D) (Fig. 4). Similar dispersions were recorded and the homogeneity of variances between raw 2D and deconvolved 3D measurements was statistically confirmed using Levene's test (Table 5). Although the medians were similar in raw 2D and deconvolved 3D, the means were significantly different in most cases (Wilcoxon test; Table 5). Raw 3D provided clearly lower values (Fig. 4). The mean SCPA measured by the classic raw 2D method was 17.23 fmol·cell^{-1}·h^{-1} in *Amphidinium* sp., 0.3786 fmol·cell^{-1}·h^{-1} in *Cyclotella* sp.1, and 32.43 fmol·cell^{-1}·h^{-1} in *Cyclotella* sp.2.

DISCUSSION

Deconvolved 3D is the best estimate

Deconvolved 3D was considered our best estimate of fluorescence intensity because it generally improved the management of out-of-focus light (which significantly increases the total measured fluorescence intensity) without introducing any detectable error. On the one hand, the biggest difference driven by deconvolution in fluorescence intensity measurements was a substantial increase in the dispersion of 2D vs. 3D measurements (Fig. 2 b relative to 2 a). Therefore, dealing with out-of-focus light (performing restorative deconvolution) is more important than correcting the eventual size effect or using raw 3D microscopy alone. The contribution of out-of-focus light to total variation in the 2D vs. 3D measurements was visibly more important (changes in overall dispersion from Fig. 2 a relative to 2 b) than that due to size effect (changes in 2D to 3D relationship between size groups in Fig. 2 a and b). Specifically, out-of-focus light may account for 4.3% of the total variation on top of the 0.03% or 0.2% due to object size. On the other hand, we showed that this difference in dispersion mainly reflected real changes in the amount of out-of-focus light per cell and therefore should not be regarded as a deconvolution artefact or a spherical aberration effect (Fig. 2 b and c, Fig 3). In summary, absolute and relative values (magnitude and dispersion) obtained by deconvolved 3D should be considered as the most reliable estimate of real values.

Raw 2D and deconvolved 3D are equivalent methods in the case of population characterization

We found that since current raw 2D quantifications do not take out-of-focus light into account, they may produce single-cell measurements that are half an order of magnitude above or below our best estimate of fluorescence intensity via deconvolved 3D.

Nevertheless, these individual errors in raw 2D measurements were partially compensated when we attempted to describe mean cell activity and functional variability of one or several species (Fig. 4) or groups of cells (Fig. 2). If 25–40 cells per species were measured in raw 2D, the obtained SD did not differ significantly from that of deconvolved 3D, and the slight (but significant) difference in means was not significantly affected by sample size either, with a confidence level of 99.99% (Table 5) (see methods for more detail). A minimum of 141 cells had to be measured to achieve a reliable result in groups of more heterogeneous cells (like a community). Thus, the measurement in raw 2D of a minimum of 25–40 cells per species provides sufficiently similar average values and ranges to deconvolved 3D.

Cell size modulates 2D measurement bias

Although deconvolved 3D was the best method tested, the results from raw 3D are also interesting since they show that cell size contributed substantially to the overall bias recorded by the raw 2D method. When object size was introduced into the model of raw 3D depending on raw 2D, adjusted R-squared (total explained variability) improved from 0.995 to 0.997. This suggests that object size modulates the raw 2D bias in relation to raw 3D. The apparent paradox is that when we modelled deconvolved 3D depending on raw 2D, the inclusion of object size did not increase the adjusted R-squared. As pointed out in the first paragraph of the discussion, we interpret this as showing that object size contributes to the fluorescence intensity bias measured in raw 2D but is clearly a less important source of variability when compared to deconvolution. These observations were essentially not undermined by having imaged under SA. According to our partial regression, comparison of raw 2D ELFA values of different species or populations of different cell sizes should be carefully interpreted: for instance, a 16 µm

diameter cell could appear to have 84% of the ELFA of a 4 μm cell in raw 2D, while they would be identical in deconvolved 3D (Table 4).

If we take raw 3D as a reference (Fig. 2 a), we can graphically observe the effect of object size on 2D fluorescence intensity measurements even when we consider this variable in discrete groups of small, medium and large cells. The simple regression lines of the three size groups showed different intercepts (relationship between 2D and 3D measurements depended on cell size). Moreover, we observed a non-linearity in this size effect: the distance between the intercepts of the regression lines of small and medium cells was greater than that between the medium and large cells (~6 μm, 14 μm and 40 μm of object diameter respectively). (Note that object sizes –the projection in the XY plane of the defined VOI– are always proportional but slightly larger than the actual cell size). Having said that object size was not the major biasing factor, we must note that most of the phytoplankton cells in oligotrophic marine and freshwater systems are frequently of small to medium size (50–52), a range in which object size bias might be more important.

Finally, deconvolution did not affect all cell sizes in the same way. When we deconvolved, the simple linear regression intercepts of all three size groups moved towards zero, but the smaller the cell, the bigger the effect of deconvolution. In this respect, the percentage of inefficient deconvolutions was the highest in larger cells. These results suggest that deconvolution may be more efficient for small and medium cells than for very large ones. Nevertheless, after checking for deconvolution efficiency, all the values of efficiently deconvolved cells were equally reliable whatever their size.

Future quantification of cells with low phosphatase activity

The fluorescence intensity measurements of weakly fluorescent objects were the most affected by deconvolution. This resulted in a quadratic relationship between deconvolved 3D and raw 2D (Fig. 1 c and d), but deconvolved 3D was the method that measured the most similar values to flow cytometry and manufacturer values for the standard 0.22% (weak fluorescence) intensity beads (Table 1). Deconvolved 3D was also reported as the most accurate quantification method for low intensity objects in the literature (35), although we did not observe such improvement. In practice, the 0.22% intensity beads recorded average fluorescence intensities (FU) like those that would produce the low ELFA amounts of: 0.35±0.07 fmol in raw 2D, 0.05±0.01 fmol in raw 3D, or 0. 92±0.45 fmol in deconvolved 3D (0.071±0.014 fmol·μm^{-2}, 0.010±0.002 fmol·μm^{-2}, and 0.187±0.092 fmol·μm^{-2} respectively). Therefore, non-linearity is a phenomenon that is restricted to the smallest values of SCHP, which constitutes a minor problem in the current state-of-the-art. Although reported SCHP values ranged from 0 to 1831 fmol·$cell^{-1}$ (53), including the non-linear range of fluorescence intensity, in current state-of-the-art, small amounts of fluorescence originating from fluorochromes in the sample other than ELFA (DAPI, degraded chlorophyll autofluorescence, etc.) may show overlap of their emission tails with the ELFA emission peak window and may account for a significant proportion when object ELFA intensity is very low. Therefore, the cells with the lowest amount of activity cannot be accurately quantified nor distinguished from completely inactive cells when DAPI or degraded chlorophyll is present in the sample. To avoid this problem, we suggest that raw 3D images should be deconvolved with an algorithm that, apart from modelling light blur, also models the spectral overlap of different fluorochromes (41). In that scenario, the question why is there a rupture of linearity between the dimmest and the intermediate fluorescent beads

when measured via deconvolved 3D in comparison to the other methods should be addressed. Such phenomenon seems to be robust because it was not only observed in this study but also in Swedlow *et al*. (35).

Improvement of the FLEA technique

One of the weaknesses that Nedoma and colleagues detected in the FLEA technique (29) was the intercalibration of a microscope with a fluorimeter, i.e., the conversion of microscope FU to fmols of ELFA. The conversion factor is the slope of a linear regression that relates the rate of ELFA formation during the linear phase of an incubation measured by a fluorimeter (in $fmol \cdot l^{-1} \cdot h^{-1}$, on the X axis) and by raw 2D image analysis (in $FU \cdot l^{-1} \cdot h^{-1}$, on the Y axis). Thus, each point on the graph represents a single incubation. The problem is that the r^2 of the regression line is about 0.65. Since the range of ELFA formation rates is already quite wide, we argue that there are other sources of the dispersion of the different incubations in the mentioned graph. Firstly, quantitative microscopy may underestimate ELFA particles <0.2 µm because the incubated sample is filtered by polycarbonate (PC) filters of the same pore size, whereas ELFA particles of all sizes are measured by fluorimetry. Thus, dispersion could be due to differences in the proportion of small ELFA particles between different incubated samples. Secondly, using raw 2D images may be another source of variability. Current raw 2D images of filters acquired to calculate the conversion factor (ConvF) are focused to the plane with the highest amount of fluorescence, but this compromise undersamples fluorescence for three reasons: only one optical slice of large objects is acquired, only one optical slice of the out-of-focus light of objects (usually >10 µm deep) is acquired, and not all objects in a frame are usually well focused because some may detach from the PC filter during sample mounting, and more important, because rippling or

mispositioning (not strictly orthogonal) of the PC filter may occur. The proposed deconvolved 3D method for FLEA quantification is expected to significantly improve this critical step in the FLEA technique.

In conclusion, deconvolved 3D FLEA measurements provide superior analytical power and are recommended to distinguish cells with SCPA differing by less than an order of magnitude. They also avoid problems of comparability between different size cells and, finally, they are the most appropriate option in those cases where the value of each single cell is important rather than the average of a population of cells. This is the case for measurements of activity in less numerous species and in the combination of the FLEA technique with other single-cell techniques. The deconvolved 3D FLEA technique alone will provide accurate information about a relevant component of trophic strategy, the enzymatic pathway, which should be incorporated into studies of biological traits that could be important for the fitness of species (54). This will aid in reconstructing the evolutionary history of the trophic strategy, defining the functional niche of many microplanktonic species, and better understanding and modelling of the dynamics of enzyme activity in nature. In addition, the deconvolved 3D FLEA technique improves the accuracy of the FLEA technique at the cell level enough to make it combinable with microautoradiography or MAR-FISH for single-cell nutrient incorporation, and with FLBs or CARD-FISH for single-cell bacterivory assessments. Such technical integrations may provide information about detailed biogeochemical processes such as the link between hydrolytic enzyme activity and nutrient uptake at the cellular level and in close-to-*in situ* conditions, but also about functional shifts in trophic strategies within mixotrophic populations of the microbial loop.

ACKNOWLEDGEMENTS

This research involved collaboration between the Limnology Group (CEAB-UB) and the Aquatic Microbial Ecology Department (HBI, CAS). We thank Dr. Jiři Nedoma for technical support during image acquisition and image analysis, and Mrs. Mireia Utzet and Dr. Francesc Carmona for statistical advice. All the authors state that we do not have any conflict of interests to declare.

REFERENCES

1. Clark LL, Ingall ED, Benner R. Marine phosphorus is selectively remineralized. Nature 1998;393:426.

2. Kolowith LC, Ingall ED, Benner R. Composition and cycling of marine organic phosphorus. Limnol. Oceanogr. 2001;46:309–320.

3. Reitzel K, Ahlgren J, Gogoll A, Jensen HS, Rydin E. Characterization of phosphorus in sequential extracts from lake sediments using P-31 nuclear magnetic resonance spectroscopy. Can. J. Fish. Aquat. Sci. 2006;63:1686–1699.

4. Bai X, Ding S, Fan C, Liu T, Shi D, Zhang L. Organic phosphorus species in surface sediments of a large, shallow, eutrophic lake, Lake Taihu, China. Environ. Pollut. 2009;157:2507–2513.

5. Luo H, Zhang H, Long R, Benner R. Depth distributions of alkaline phosphatase and phosphonate utilization genes in the North Pacific Subtropical Gyre. Aquat. Microb. Ecol. 2011;62:61–69.

6. Schindler DW. Evolution of Phosphorus Limitation in Lakes. Science 1977;195:260–262.

7. Thingstad TF, Rassoulzadegan F. Nutrient limitations, microbial food webs, and biological C-pumps - Suggested interactions in a P-limited Mediterranean. Mar. Ecol. Prog. Ser. 1995;117:299–306.

8. Perry MJ. Phosphate utilization by an oceanic diatom in phosphorus-limited chemostat culture and in the oligotrophic waters of the central North Pacific. Limnol. Oceanogr. 1976;21:88–107.

9. Vidal M, Duarte CM, Agustí S, Gasol JM, Vaqué D. Alkaline phosphatase activities in the central Atlantic Ocean indicate large areas with phosphorus deficiency. Mar. Ecol. Prog. Ser. 2003;262:43–53.

10. Reich PB, Oleksyn J. Global patterns of plant leaf N and P in relation to temperature and latitude. Proc. Natl. Acad. Sci. U. S. A. 2004;101:11001–11006.

11. Elser JJ, Andersen T, Baron JS, Bergström A-K, Jansson M, Kyle M, Nydick KR, Steger L, Hessen DO. Shifts in lake N:P stoichiometry and nutrient limitation driven by atmospheric nitrogen deposition. Science 2009;326:835–837.

12. Sinsabaugh RL, Carreiro MM, Repert DA. Allocation of extracellular enzymatic activity in relation to litter composition, N deposition, and mass loss. Biogeochemistry 2002;60:1–24.

13. Edwards I, Zak D, Kellner H, Eisenlord S, Pregitzer K. Simulated Atmospheric N Deposition Alters Fungal Community Composition and Suppresses Ligninolytic Gene Expression in a Northern Hardwood Forest. PLoS One 2011;6:1-10.

14. Yamada N, Tsurushima N, Suzumura M. Effects of Seawater Acidification by Ocean CO(2) Sequestration on Bathypelagic Prokaryote Activities. J. Oceanogr. 2010;66:571–580.

15. Piontek J, Lunau M, Haendel N, Borchard C, Wurst M. Acidification increases microbial polysaccharide degradation in the ocean. Biogeosciences 2010;7:1615–1624.

16. Sardans J, Penuelas J, Estiarte M. Seasonal patterns of root-surface phosphatase activities in a Mediterranean shrubland. Responses to experimental warming and drought. Biol. Fertil. Soils 2007;43:779–786.

17. Wallenstein M, Allison S, Ernakovich J, Steinweg JM, Sinsabaugh R. Controls on the Temperature Sensitivity of Soil Enzymes: A Key Driver of In Situ Enzyme Activity Rates. Soil Biol. 2011;22:245–258.

18. Boavida M-JJ, Wetzel RG. Inhibition of phosphatase activity by dissolved humic substances and hydrolytic reactivation by natural ultraviolet light. Freshw. Biol. 1998;40:285–293.

19. Espeland EMM, Wetzel RGG. Complexation, stabilization, and UV photolysis of extracellular and surface-bound glucosidase and alkaline phosphatase: Implications for biofilm microbiota. Microb. Ecol. 2001;42:572–585.

20. Tank SE, Xenopoulos MA, Hendzel LL. Effect of ultraviolet radiation on alkaline phosphatase activity and planktonic phosphorus acquisition in Canadian boreal shield lakes. Limnol. Oceanogr. 2005;50:1345–1351.

21. Steen AD, Arnosti C. Long lifetimes of beta-glucosidase, leucine aminopeptidase, and phosphatase in Arctic seawater. Mar. Chem. 2011;123:127–132.

22. González-Gil S, Keafer BA, Jovine RVM, Aguilera A, Lu S, Anderson DM. Detection and quantification of alkaline phosphatase in single cells of phosphorus-starved marine phytoplankton. Mar. Ecol. Prog. Ser. 1998;164:21–35.

23. Lauro F, McDougald D, Thomas T, Williams T, Egan S. The genomic basis of trophic strategy in marine bacteria. Proc. Natl. Acad. Sci. U. S. A. 2009;106:15527–15533.

24. Christie-Oleza JA, Piña-Villalonga JM, Bosch R, Nogales B, Armengaud J. Comparative proteogenomics of twelve Roseobacter exoproteomes reveals different adaptive strategies among these marine bacteria. Mol. Cell. proteomics 2012;11:1–12.

25. Ou L, Huang B, Lin L, Hong H, Zhang F, Chen Z. Phosphorus stress of phytoplankton in the Taiwan Strait determined by bulk and single-cell alkaline phosphatase activity assays. Mar. Ecol. Ser. 2006;327:95–106.

26. Carlsson P, Caron DA. Seasonal variation of phosphorus limitation of bacterial growth in a small lake. Limnol. Oceanogr. 2001;46:108–120.

27. Nedoma J, Vrba J. Specific activity of cell-surface acid phosphatase in different bacterioplankton morphotypes in an acidified mountain lake. Environ. Microbiol. 2006;8:1271–1279.

28. Duhamel S, Gregori G, Van Wambeke F, Nedoma J. Detection of Extracellular Phosphatase Activity at the Single-Cell Level by Enzyme-Labeled Fluorescence and Flow Cytometry: The Importance of Time Kinetics in ELFA Labeling. Cytom. Part A 2009;75A:163–168.

29. Nedoma JJ, Štrojsová A, Vrba J, Komárková J, Šimek K, Strojsova A, Komarkova J, Simek K. Extracellular phosphatase activity of natural plankton studied with ELF97 phosphate: fluorescence quantification and labelling kinetics. Environ. Microbiol. 2003;5:462–472.

30. Litchman E, Klausmeier CA. Trait-Based Community Ecology of Phytoplankton. Annu. Rev. Ecol. Evol. Syst. 2008;39:615–639.

31. Litchman E, Klausmeier CA, Schofield OM, Falkowski PG. The role of functional traits and trade-offs in structuring phytoplankton communities: scaling from cellular to ecosystem level. Ecol. Lett. 2007;10:1170–1181.

32. Allison SD. A trait-based approach for modelling microbial litter decomposition. Ecol. Lett. 2012;15:1058–1070.

33. Andrews PD, Harper IS, Swedlow JR. To 5D and beyond: Quantitative fluorescence microscopy in the postgenomic era. Traffic 2002;3:29–36.

34. Verveer PJ, Gemkow MJ, Jovin TM. A comparison of image restoration approaches applied to three-dimensional confocal and wide-field fluorescence microscopy. J. Microsc. 1999;193:50–61.

35. Swedlow JR, Hu K, Andrews PD, Roos DS, Murray JM. Measuring tubulin content in Toxoplasma gondii: A comparison of laser-scanning confocal and wide-field fluorescence microscopy. Proc. Natl. Acad. Sci. 2002;99:2014–2019.

36. Murray JM, Appleton PL, Swedlow JR, Waters JC. Evaluating performance in three-dimensional fluorescence microscopy. J. Microsc. 2007;228:390–405.

37. Barlow AL, Guerin CJ. Quantization of widefield fluorescence images using structured illumination and image analysis software. Microsc. Res. Tech. 2007;70:76–84.

38. Wallace W, Schaefer LH, Swedlow JR. A workingperson's guide to deconvolution in light microscopy. Biotechniques 2001;31:1076–1097.

39. McNally JG, Karpova T, Cooper J, Conchello JA. Three-Dimensional Imaging by Deconvolution Microscopy. Methods 1999;19:373–385.

40. Swedlow JR. Quantitative fluorescence microscopy and image deconvolution. Methods Cell Biol. 2007;81:447–465.

41. Hoppe AD, Swanson J a., Shorte SL. Three-dimensional FRET microscopy Periasamy A, So PTC, editors. Proc. SPIE--the Int. Soc. Opt. Eng. 2006;6089:1–9.

42. Selinummi J, Niemisto A, Saleem R, Carter G, Aitchison J, Yli-Harja O. A case study on 3D reconstruction and shape description of peroxisomes in yeast. 2007 IEEE Int. Conf. Signal Process. Commun. 2008:672–675.

43. Huang K, Murphy RF. From quantitative microscopy to automated image understanding. J. Biomed. Opt. 2004;9:893–912.

44. Diaz-de-Quijano D, Felip M. A comparative study of fluorescence-labelled enzyme activity methods for assaying phosphatase activity in phytoplankton. A possible bias in the enzymatic pathway estimations. J. Microbiol. Methods 2011;86:104–7.

45. Davison AC, Hinkley D V. Bootstrap methods and their application. Cambridge: Cambridge University Press; 1997:582.

46. Crawley MJ. Regression. Bootstrap with regression. In: R B. Chichester: John Wiley & Sons, Ltd.; 2007. p 418–421.

47. Model MA, Burkhardt JK. A standard for calibration and shading correction of a fluorescence microscope. Cytometry 2001;44:309–316.

48. Hiraoka Y, Sedat JW, Agard DA. The use of a charge-coupled device for quantitative optical microscopy of biological structures. Science 1987;238:36–41.

49. R_Development_Core_Team. R: A Language and Environment for Statistical Computing Team RDC, editor. R Found. Stat. Comput. 2011;1:409.

50. Duarte CM, Agustí S, Canfield DE. Size plasticity of fresh-water pytoplankton: Implications for community structure. Limnol. Oceanogr. 1990;35:1846–1851.

51. Sarmento H. New paradigms in tropical limnology: the importance of the microbial food web. Hydrobiologia 2012;686:1–14.

52. Chen B, Liu H. Relationships between phytoplankton growth and cell size in surface oceans: Interactive effects of temperature, nutrients, and grazing. Limnol. Oceanogr. 2010;55:965–972.

53. Novotná J, Nedbalová L, Kopáček J, Vrba J. Cell-specific extracellular phosphatase activity of Dinoflagellate populations in acidified mountain lakes. J. Phycol. 2010;46:635–644.

54. Green JL, Bohannan BJM, Whitaker RJ. Microbial biogeography: From taxonomy to traits. Science 2008;320:1039–1043.

	Manufacturer	Flow cytometry	Raw 2D		Raw 3D		Deconvolved 3D	
n	Fluorescence Intensity (%)	Fluorescence Intensity (%)	Fluorescence Intensity (FU) and (SD)	Fluorescence Intensity (%)	Fluorescence Intensity (FU) and (SD)	Fluorescence Intensity (%)	Fluorescence Intensity (FU) and (SD)	Fluorescence Intensity (%)
37	100	100	19719 (1879)	100	202750 (26123)	100	18226411 (16718390)	100
29	38	36	6068 (541)	30.11	64803 (6959)	30.91	9467089 (1966014)	29.47
36	14	13	2110 (172)	10.57	22033 (1828)	10.66	2637021.8 (1333435)	9.83
22	3.3	3.1	547 (28.3)	2.75	5739 (431)	2.81	636586 (437252)	2.73
36	0.96	0.9	157 (14.7)	0.79	1679 (149)	0.82	168243 (114843)	0.75
33	0.25	0.22	25.6 (4.9)	0.18	371 (49.1)	0.18	65583 (32185)	0.24

Table 1. Average fluorescence intensities of the different groups of fluorescence intensity standard beads. Values are in percentage relative to the most fluorescent group, and in fluorescence units (FU). Note that values, in FU, increase one order of magnitude from raw 2D to raw 3D, and two orders of magnitude more from raw 3D to deconvolved 3D.

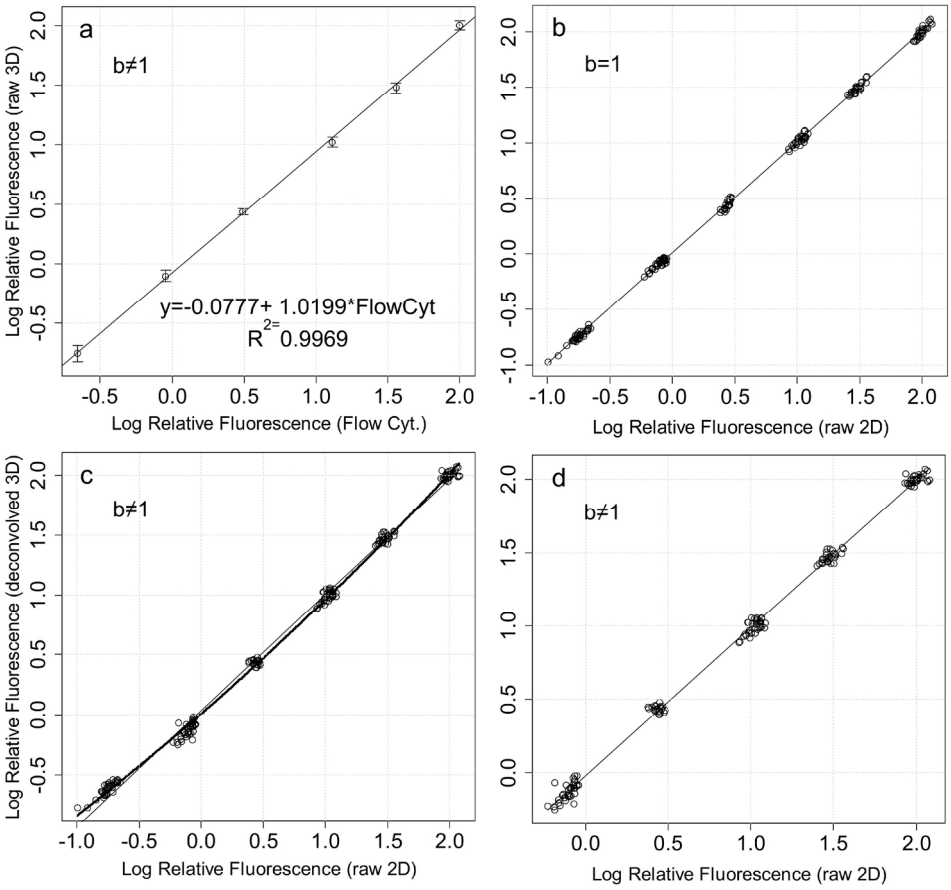

Fig. 1. Comparison of standard fluorescence intensity bead measurements performed using different methods (flow cytometry and quantitative microscopy: raw 2D, raw 3D and deconvolved 3D). Thin lines are linear regressions, thick line in Figure c is quadratic regression. Figure d presents the same data as c, but excluding the lowest intensity fluorescent beads.

175x181mm (300 x 300 DPI)

Slopes	2.5 µm	6 µm	15.4 µm
Raw 2D vs. Raw 3D	10.23 (10.09, 10.41)	15.31 (13.98, 16.92)	20.77 (20.51, 21.04)
Raw 2D vs. Dec. 3D	18.92 (18.07, 19.71)	23.98 (16.43, 30.99)	43.31 (22.53, 56.88)

Table 2. Slopes of linear regressions relating 2D and 3D measurements of fluorescent beads of different sizes. In brackets are the bootstrapped 95% confidence intervals of these slopes. The bootstrapped confidence intervals are of the bias-corrected accelerated percentile (Bca) type and are based on 10,000 bootstrap replicates (see experimental procedures for more detail).

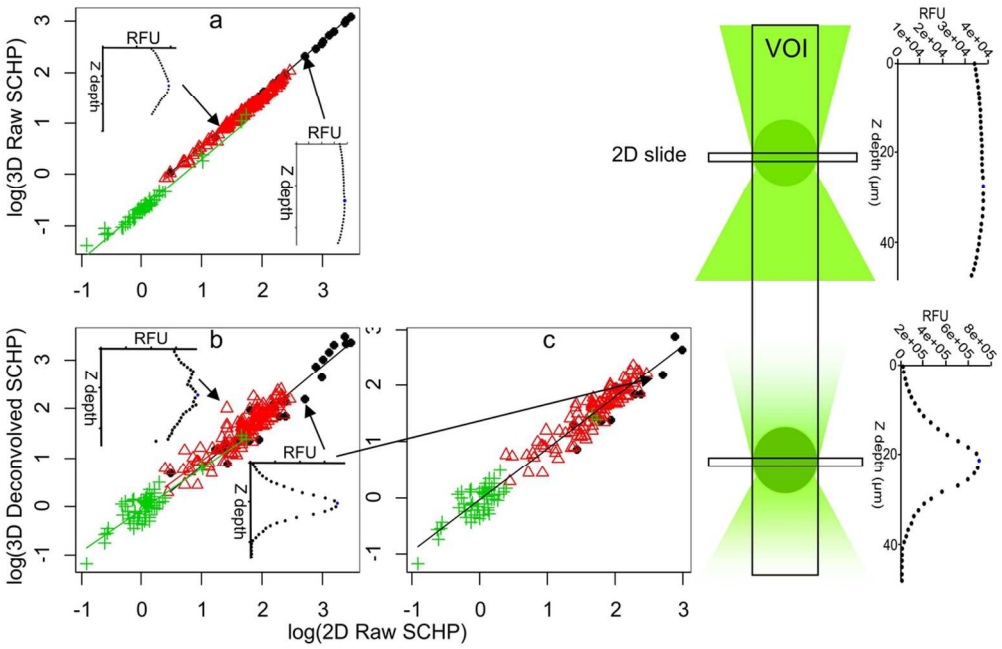

Fig. 2. Right: Schema of the lateral view of a raw cell (top) and a well deconvolved cell (bottom), and their respective intensity profiles. Horizontal rectangles represent in-focus 2D slides, the vertical one represents the volume of interest (VOI) for 3D fluorescence measurements. Left: Comparison of three different IA fluorescence quantification methods using the log of SCHP (fmol ELFA·cell^{-1}) of phytoplankton cells (a and b). Graph c is the same as graph b but excludes inefficient deconvolved cells. Small (green cross), medium (red triangle), and large cells (black circle). The intensity profiles of a well deconvolved cell and an inefficiently deconvolved cell are embedded in graphs a (raw) and b (deconvolved profiles). The arrows point out the position of these two example cells.
109x70mm (300 x 300 DPI)

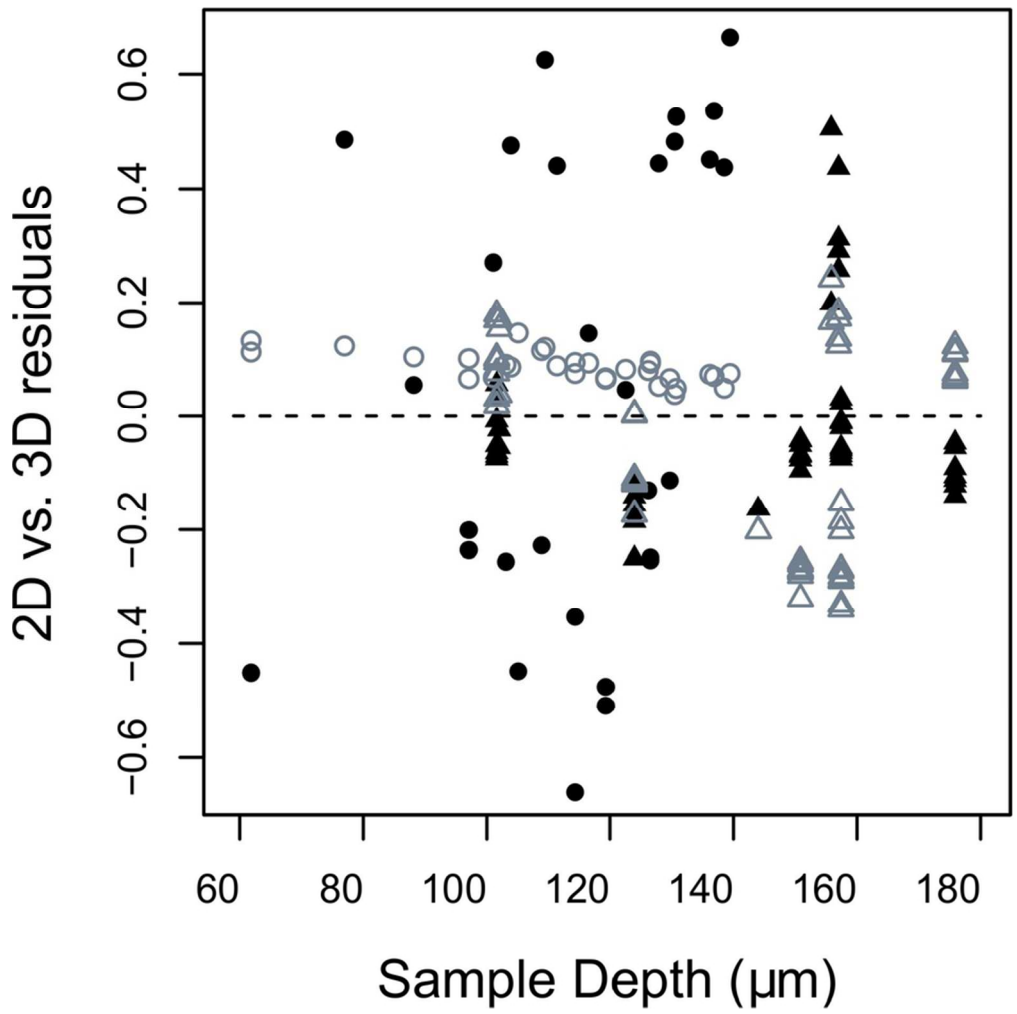

Fig. 3 Relationship between sample depth (or distance to the coverslide) of 2.5 μm (triangles) and 15 μm (circles) fluorescent beads, and the residuals of linear regressions relating their raw 2D and raw 3D (grey) or raw 2D and deconvolved 3D (black) fluorescence intensities.
80x80mm (300 x 300 DPI)

	Variation explained by Raw 2D	Variation explained by Raw 2D and Area	Variation explained by Area	Unexplained variation
Raw 3D	33.5%	66.1%	0.2%	0.2%
Deconvolved 3D	28.9%	66.6%	0.03%	4.5%

Table 3. Proportions of variation of raw and deconvolved 3D values (R^2).

	32 µm	16 µm	8 µm	4 µm	2 µm
32 µm	100	109	119	130	142
16 µm	92	100	109	119	130
8 µm	84	92	100	109	119
4 µm	77	84	92	100	109
2 µm	71	77	84	92	100

Table 4. Percentage between the apparent raw 2D SCHP simulated for five ideal spherical cells (from 2 to 32 µm diameter) with the same deconvolved 3D SCHP value. The table is to be read from columns to rows. For instance: in raw 2D SCHP values, a 2µm diameter cell seems to have a 142% of the ELFA of a 32µm cell with the same deconvolved 3D SCHP value. Inversely, a 32µm cell seems to have the 71% of the ELFA of a 2µm cell with the same deconvolved 3D SCHP value.

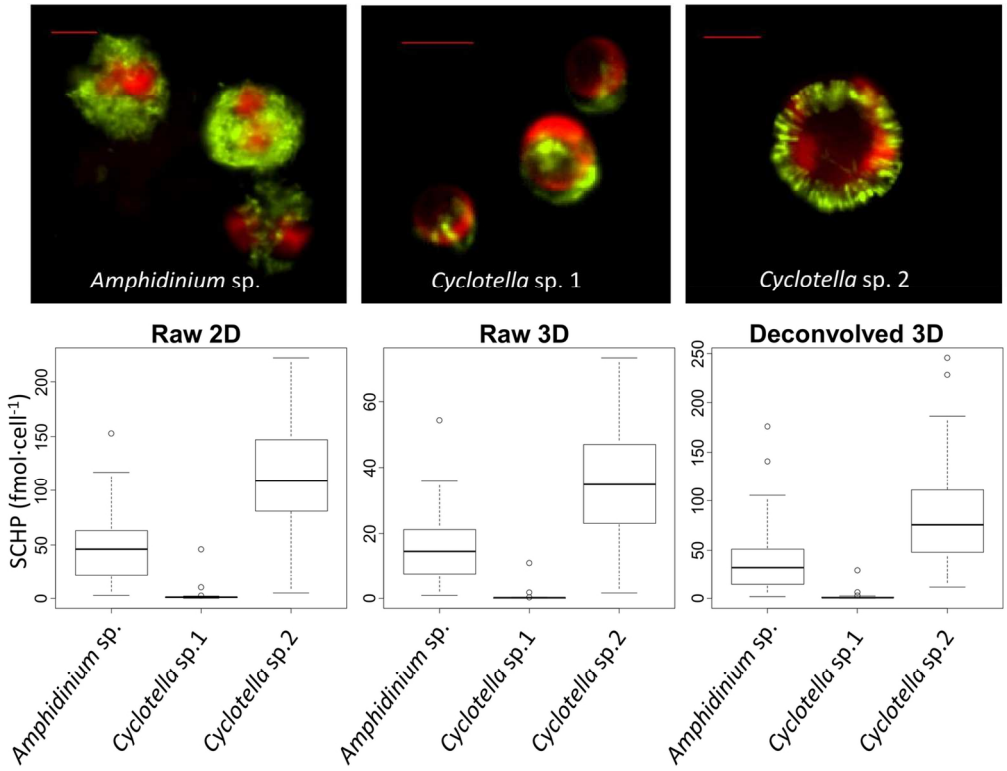

Fig. 4. Epifluorescence microimages of three phytoplankton species. Red: chloroplasts; Yellow-green: ELFA precipitates indicating phosphatase activity. Scale bars are 5 µm long. Single cell hydrolysed phosphate (SCHP) of the three separate phytoplankton populations, measured using the three IA quantification methods.
130x100mm (300 x 300 DPI)

n	Species	Size	Mean (p-v)	SD (p-v)	Minimum sampling size (number of cells)
175	All	All	$\neq (3.075\times10^{-14})$	= (0.4598)	141
53	*Amphidinium* sp.	Medium (14µm)	≠ (0.0004)	= (0.8421)	39
54	*Cyclotella* sp.1	Small (~6µm)	= (0.0761)	= (0.6858)	37
35	*Cyclotella* sp.2	Medium (14µm)	$\neq (1.106\times10^{-9})$	= (0.1360)	26

Table 5. Wilcoxon and Levene tests for comparison of means and homogeneity of variances between raw 2D and deconvolved 3D fluorescence intensity measurements in the three selected species and the whole set of efficiently deconvolved cells.

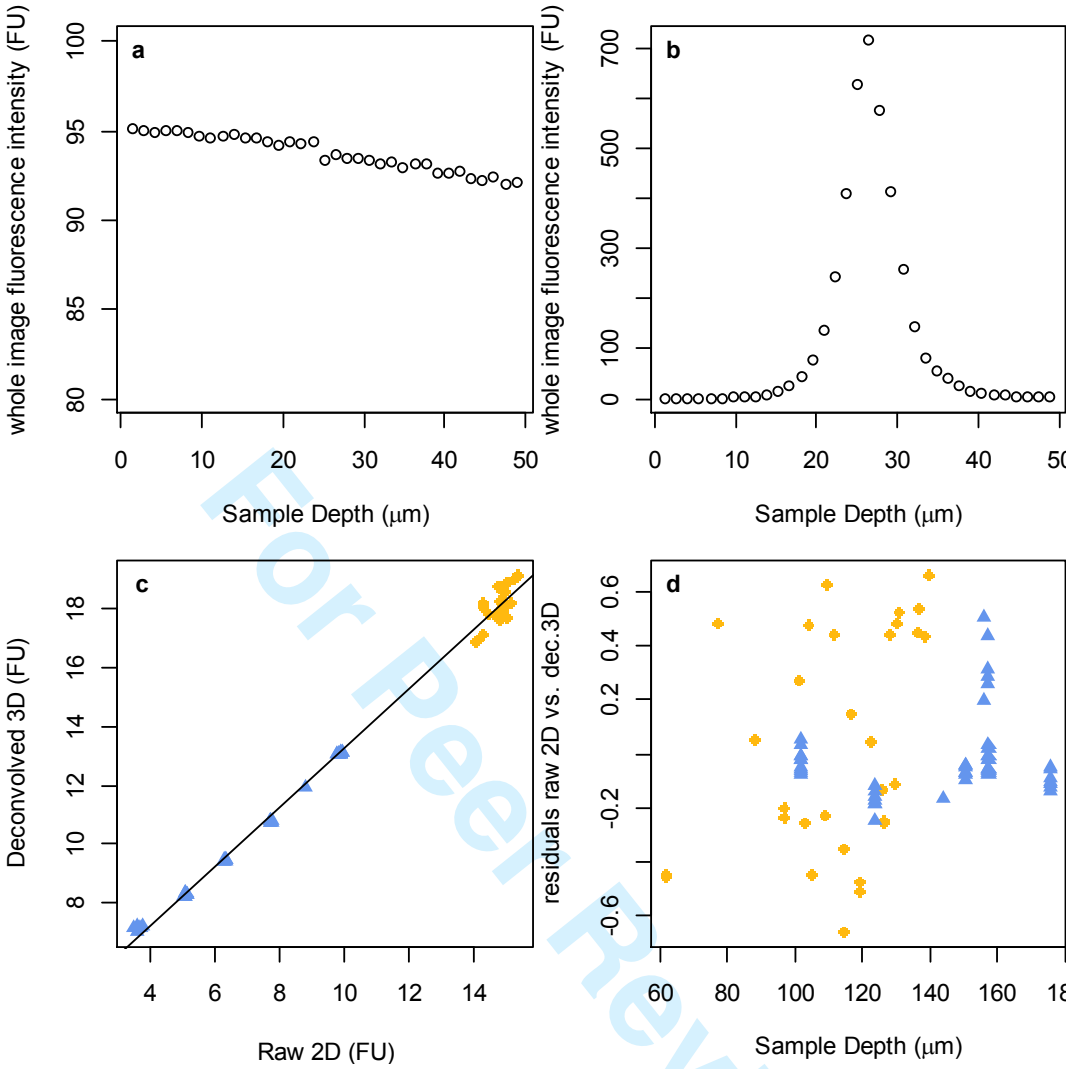

Fig. 5 Fluorescence intensity profiles of a phytoplankton cell based on a whole raw image (a) and a whole deconvolved image(b). Relationship between several fluorescence intensity parameters and object distance to the coverslide in 2.5µm (blue triangles) and 15µm (yellow circles) fluorescent beads.

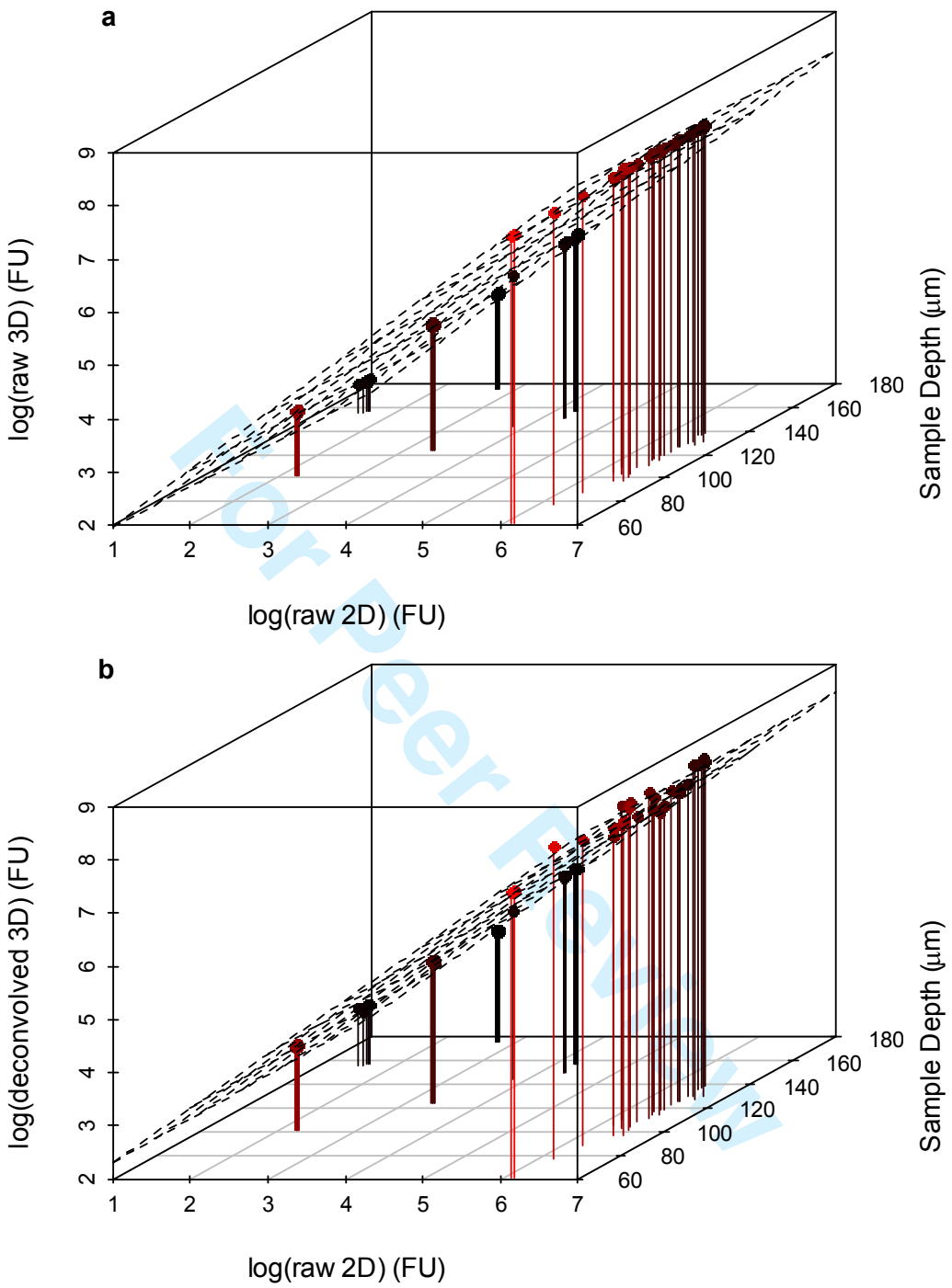

Fig. 6 Fluorescence intensity measurements of small (2.5µm) and big (15µm) beads in 2D and raw 3D (a) or deconvolved 3D (b) methods versus the distance of the in-focus slide to the coverslide (sample depth). The red to black gradation represents individuals in shallow to deep sample depth. Note that the increase in dispersion when deconvolving does not correlate to sample depth.

Cytometry Part A
Author Checklist: MIFlowCyt-Compliant Items

Requirement	Please Include Requested Information
1.1. Purpose	To detect a set of fluorescent beads by flow cytometry to compare their relative fluorescence intensity to that measured by epifluorescence microscopy
1.2. Keywords	Beads, fluorescence, microscopy
1.3. Experiment variables	Relative fluorescence intensities of intensity calibrated fluorescent beads
1.4. Organization name and address	Biology Centre AS CR, Institute of Hydrobiology, Na Sadkach 7, 37005 Ceske Budejovice, Czech Republic
1.5. Primary contact name and email address	Karel Hornak, khornak1@gmail.com
1.6. Date or time period of experiment	26th Feb 2009
1.7. Conclusions	Analyses of fluorescence intensities of the beads by flow cytometry proved to be a sensitive, rapid and equally sensitive method as compared to epifluorescence microscopy
1.8. Quality control measures	TruCount beads (BD) were used as an internal standard to check for fluorescence intensities
2.1.1.1. (2.1.2.1., 2.1.3.1.) Sample description	Intensity calibrated fluorescent beads diluted in ultra-pure water
2.1.1.2. Biological sample source description	Intensity calibrated fluorescent beads diluted in ultra-pure water
2.1.1.3. Biological sample source organism description	Not applicable
2.1.2.2. Environmental sample location	Not applicable
2.3. Sample treatment description	Fluorescent beads (details below) were diluted in ultra-pure water and immediately analysed by flow cytometry
2.4. Fluorescence reagent(s) description	2.5 µm diameter fluorescence intensity calibrated beads (In Speck™ Green (505/515) Microscope Image Intensity Calibration Kit, 2.5 Um, Invitrogen, Molecular Probes, I7219).
3.1. Instrument manufacturer	Becton Dickinson, USA
3.2. Instrument model	BD FACSCalibur equipped with an air-cooled argon ion laser (15 mW, 488 nm) and with a standard set of filters
3.3. Instrument configuration and settings	All samples were analysed using the following setting: SSC detector voltage 450, FL1 detector voltage 425, both in a log amplification mode
4.1. List-mode data files	1) The link for peer-review process: http://flowrepository.org/id/RvFrufapJNm6aYKbqI6gIGoymAAECrAB5l7SiEmLYhNF4xQRgDh2eRzWo3KzNx1d 2) The repository identifier: http://flowrepository.org/id/FR-FCM-ZZBL
4.2. Compensation description	No compensation
4.3. Data transformation details	No transformation
4.4.1. Gate description	6 different subpopulations of beads with distinct fluorescence intensities were unambiguously discriminated in the SSC (light scatter) vs. FL1 (515 nm) plot based on their fluorescence signatures.
4.4.2. Gate statistics	Percentage and relative fluorescence intensities (FL1, 515 nm) of each of the subpopulations as defined by the respective gates.
4.4.3. Gate boundaries	No overlapping gates were detected.

Notes

Feel free to use more space than allocated.

You can embed graphics/figures in this document, if needed.

Please make sure to save the document in Microsoft Word version 2003 or older, before uploading to ScholarOne Manuscripts. When uploading this checklist to ScholarOne Manuscripts, please choose the "Supplementary Material for Review" category.

Please note that if your paper is accepted, the checklist will be published as an Online Supporting Information.

For any questions, please contact the Cytometry Part A editorial office at Cytometrya@wiley.com.

File: beads-mix-26-02-09 Sample ID: beads-mix-26-02-09
Acquisition Date: 26-Feb-09 Gated Events: 163500
Total Events: 163500

Marker	Events	% Total	Mean	Geo Mean	SD	CV	Median	Peak	Peak Ch
All	163500	100.00	586.77	116.62	1231.04	209.80	148.55	2905	159
100%	10646	6.51	4957.07	4951.89	223.03	4.50	5002.86	1220	5093
~30%	7968	4.87	1792.41	1790.63	78.44	4.38	1810.56	1175	1843
~10%	28792	17.61	634.23	633.21	35.85	5.65	637.80	1876	661
~3%	50824	31.09	152.00	151.74	8.72	5.73	152.61	2905	159
~1%	37967	23.22	45.64	45.59	2.26	4.96	45.73	2508	46
~0.3%	12099	7.40	11.81	11.79	0.75	6.35	11.86	699	11

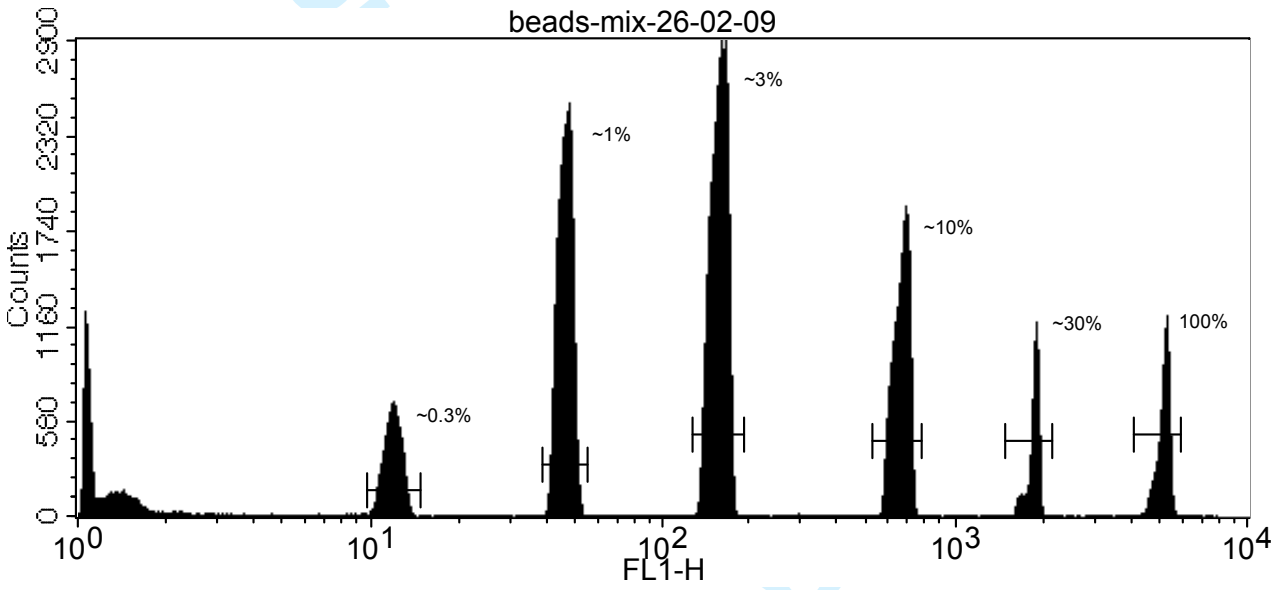

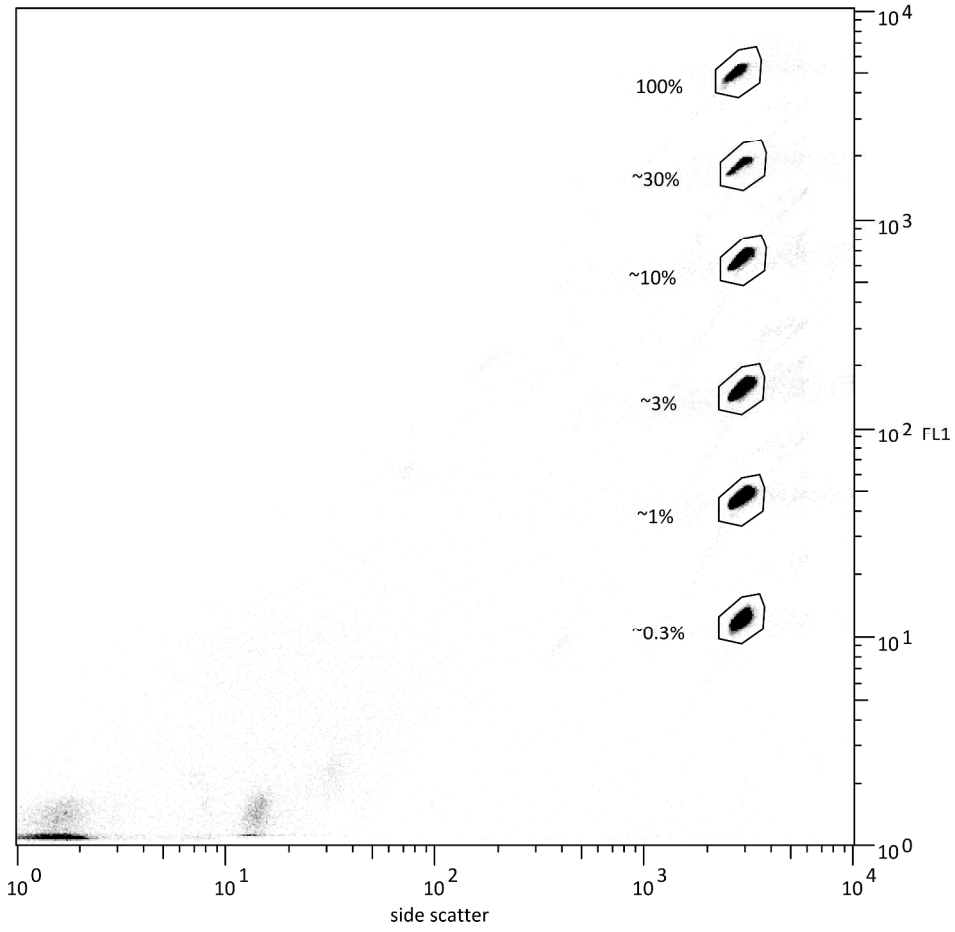

Dotplot showing the gating strategy of fluorescence calibrated beads
1253x1220mm (96 x 96 DPI)